

# The photon scattering cross-sections of atomic hydrogen

Swaantje J. Grunefeld and Michael W. J. Bromley\*

*School of Mathematics and Physics, The University of Queensland, Brisbane, St Lucia, QLD 4072, Australia*

Yongjun Cheng

*Academy of Fundamental and Interdisciplinary Science,  
Harbin Institute of Technology, Harbin 150080, PR China and  
School of Engineering, Charles Darwin University, Darwin NT 0909, Australia*

(Dated: June 6, 2016)

We present a unified view of the frequency dependence of the various scattering processes involved when a neutral hydrogen atom interacts with a monochromatic, linearly-polarized photon. A computational approach is employed of the atom trapped by a finite-sized-box due to a finite basis-set expansion, which generates a set of transition matrix elements between  $E < 0$  eigenstates and  $E > 0$  pseudostates. We introduce a general computational methodology that enables the computation of the frequency-dependent dipole transition polarizability with one real and two different imaginary contributions. These dipole transition polarizabilities are related to the cross-sections of one-photon photoionization, Rayleigh, Raman, and Compton scattering. Our numerical calculations reveal individual Raman scattering cross-sections above threshold that can rapidly vanish and revive. Furthermore, our numerical Compton cross-sections do not overtly suffer from the infra-red divergence problem, and are three orders-of-magnitude higher than previous analytic-based Compton scattering cross-sections. Our total photon-hydrogen scattering cross-sections thus resolve the discrepancies between these previous calculations and those in the N.I.S.T. ‘FFAST’ database.

PACS numbers: 31.15.ap, 32.30.-r, 32.80.Fb

The problem of photon-atom scattering was first tackled using quantum theory in the mid-to-late 1920s, resulting in the development of the Kramers-Heisenberg-Waller matrix elements [1]. These describe the fundamental Rayleigh and Raman processes, however, are also known to suffer from an infra-red divergence problem when computing Compton scattering cross-sections [2]. In this paper we avoid this problem by building a computational photon-plus-atom-in-a-box, which effectively results in an upper photon wavelength based on the size of the box, and we are able to obtain the total photon-hydrogen scattering cross-sections.

The real and two different imaginary dipole transition polarizabilities are set up in the present methodology and used to compute the set of non-relativistic low-frequency photon-hydrogen cross-sections. The incident photon field *strengths* are assumed to lie in the weak-to-intermediate regime where a collision involving two-incident photons are unlikely, and where second-order perturbative treatments of a photon-atom collision are applicable [3]. Photon-atomic hydrogen experiments are notoriously challenging [4]. Previously three-photon ionization experiments have been performed [5], and recently experiments have been performed further into the strong-field regime using ultrafast laser pulses [6], neither of which do we attempt to connect our results to since (high-order perturbative) multiphoton treatments are required.

The fundamental computational approach taken in this

paper to compute the cross-sections is to use the transition matrix elements connecting two states via a complete set of intermediate states summed over both bound eigenstates and pseudostates. These are schematically shown in Fig. 1 for the cases of Rayleigh and Compton scattering where an  $\ell = 1$  state is given as an example of the intermediate state and some possible dipole decay pathways from this state are also shown that would impact the transition linewidth. We present cross-sections here without resolving either fine or hyperfine structure, which in future work could be included [7].

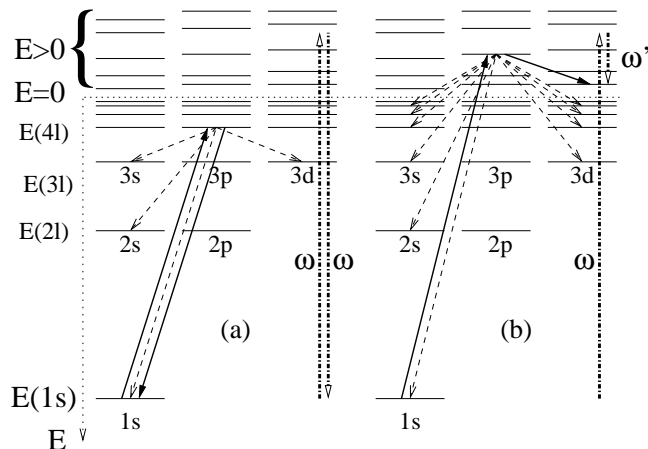
This paper was initially motivated by the incompleteness in the compiled set of theoretical photon-hydrogen total cross-sections in Fig. 29 of Bergstrom *et al.* [8]. There they did not present Raman scattering cross-sections, whilst Compton cross-sections were presented over a limited frequency range based on a low-energy (infra-red) photon truncation of the analytic differential cross-sections from Gavrilin [9–11]. They consequently noted that “the total Compton cross-section does not continue to fall at low energies” [8] as one would predict.

This problem was more recently tackled by Drukarev *et al.* [12], who also used the work of Gavrilin, and also an approximation to numerically avoid the infra-red divergence. Their total Compton cross-section does fall at low energies, however, their highest-energy cross-sections at 100 eV are mismatched by an order-of-magnitude against those in Ref. [8]. Both of these calculations, furthermore, lie vastly below those in the “FFAST: Form Factor, Attenuation, & Scattering Tables” computed by Chantler [13]. The FFAST database covers all atoms and are used for a variety of applications spanning medical and materials science applications [14, 15]. Our results in

---

\*URL: [www.smp.uq.edu.au/people/brom/](http://www.smp.uq.edu.au/people/brom/)

FIG. 1: Schematic of some photon scattering processes from the hydrogen  $1s$  state. The incoming photon frequency,  $\omega$ , is depicted here as lying above the ionization threshold. Series (a) indicates Rayleigh scattering where one of the perturbative terms involves the physical ( $4p$ ) eigenstate with the absorption / spontaneous emission of an  $\omega$  photon. The allowed dipole decays from the  $4p$  state are shown in dashed-lines. Series (b) shows Compton scattering, where one of the perturbative terms involves an  $E > 0$   $\ell = 1$  pseudostate, and then spontaneous decay of frequency  $\omega'$  shown down into a  $\ell = 2$  pseudostate (which would subsequently ionize). Some allowed dipole decays from the  $\ell = 1$  pseudostate are shown in dashed-lines. These impact the linewidths of these processes (during Compton scattering the final  $\ell = 2$  pseudostate would also have a number of decay channels that impacts its linewidth).



this paper are qualitatively similar to, yet 30–60% larger than, the FFAST scattering cross-sections, and this is just for the neutral hydrogen atom.

*Photon-Atom Methodology* — Our numerical method begins by diagonalizing our hydrogen atom using a finite-sized (orthogonal) Laguerre basis set that provides some kind of a soft-walled potential atom-in-a-box [16]. This discretizes the continuum and provides both bound state and ‘pseudostate’ information that can be used to compute frequency-dependent polarizabilities below the ionization threshold [17, 18], and for dispersion coefficients [19]. The pseudostate information can also be exploited to perform, eg. lepton-atom scattering [16, 20]. The use of pseudostates for above threshold photon-atom scattering was explored by Langhoff *et al.* for Rayleigh scattering and one-photon photoionization [21–25].

We extend these methods to also perform calculations of Raman scattering and, furthermore, of Compton scattering. The photon-atom scattering cross-sections are based on the Kramers-Heisenberg-Waller matrix elements involving the electromagnetic coupling  $H_c = (2mc^2)^{-1}e^2A^2 - (mc)^{-1}e\vec{p} \cdot \vec{A}$  [1, 2]. We ignore the  $A^2$  ‘seagull’ term (the Waller matrix element) since that is only important at  $\gtrsim$  keV photon energies [8, 26]. The Kramers-Heisenberg matrix element is determined here as a transition polarizability,  $\alpha_{ji}(\omega)$ , between some initial

state  $|i; L_i S\rangle$  and final state  $|j; L_j S\rangle$  through a complete set of intermediate states  $|t; L_t S\rangle$  [27]. The details of our algorithms are given in the Supplemental Material, Sections I and II. In brief, we use reduced matrix elements, assuming linear polarization [7, 28], such that

$$\alpha_{ji}(\omega) \approx \sum_t C_{L_i, L_t, L_j} \left[ \frac{\langle j || z || t \rangle \langle t || z || i \rangle}{\varepsilon_{ti} - \omega - i\frac{1}{2}\Gamma_{ti}(\omega)} + \frac{\langle j || z || t \rangle \langle t || z || i \rangle}{\varepsilon_{tj} - (-\omega) - i\frac{1}{2}\Gamma_{tj}(\omega)} \right], \quad (1)$$

where  $\varepsilon_{ab} = E_b - E_a$ , and all quantities above are in atomic units (a.u.). We use the expressions in Ref. [7], to find that  $C_{0,1,0} = \frac{1}{3}$ , whilst  $C_{0,1,2} = \frac{1}{3}$ .

Each  $\alpha_{ji}(\omega)$  is calculated as a sum over intermediate states  $t$ , which are either bound or pseudostates. When the intermediate state is a bound state, we compute an imaginary term (denoted  $\text{Im}_0$ ) by the damping of the oscillator through the linewidth/s of the atomic bound states [2, 28–30]. Wijers has argued [31] that the decay rates must be frequency dependent to ensure  $\Gamma_{ab}(\omega) \rightarrow 0$  as  $\omega \rightarrow 0$ . Thus we use  $\Gamma_{ab}(\omega) = (\Gamma_a + \Gamma_b)(2\varepsilon_{ab}^2\omega^2 / (\varepsilon_{ab}^4 + \omega^4))$ . This form of the resonant damping includes the case where the state that absorbs the photon has a non-zero decay rate to other bound states.

If the intermediate state in Eqn. 1 is a pseudostate, then the linewidth is not included as continuum states do not have a physical linewidth. For  $\omega > |E_{1s}|$ , this results in unphysical singularities in the continuum when  $\omega = \varepsilon_{ti}$ . These are removed by assuming infinitesimally small pseudostate linewidths  $\Gamma_{ti} \rightarrow 0^+$ , which results in real and imaginary (denoted  $\text{Im}_1$ ) terms [23]. This enables us to compute one real and the two different imaginary polarizabilities. Our calculations of  $\alpha_{ji}$  where  $i \equiv 1s$  were all performed with a fixed number of Laguerre-type orbitals  $N_\ell = 120$  for each angular momentum, which gives 18  $\ell = 1$  ( $E < 0$ ) bound states and 102  $\ell = 1$  ( $E > 0$ ) pseudostates. Convergence studies against other basis sets are relegated to Supplemental Section IV.

*Cross-section results* — For (elastic) Rayleigh scattering of a photon with frequency  $\omega$  we have [7, 23, 33]

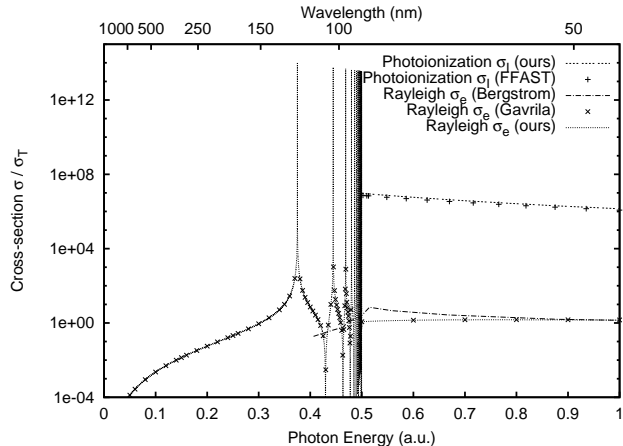
$$\sigma_e(\omega) = \sigma_T \omega^4 \left| \text{Re}[\alpha_{ii}(\omega)] + i\text{Im}_0[\alpha_{ii}(\omega)] \right|^2, \quad (2)$$

where  $\sigma_T$  is the Thomson scattering cross-section of a photon with a free electron (for reference,  $\sigma_T \approx 6.65 \times 10^{-25}$  cm<sup>2</sup>), whilst  $\omega$  and  $\alpha_{ii}$  are both in a.u.. The photoionization cross-section is given by [24]

$$\sigma_I(\omega) = \sigma_T \frac{3}{2} c^3 \omega \text{Im}_1[\alpha_{ii}(\omega)], \quad (3)$$

i.e. the optical theorem. The speed-of-light,  $c \approx 137$  (in a.u.), gives the massive enhancement factor of  $\sigma_I$  over that of  $\sigma_e$ . Our results for these cross-sections for validation purposes are shown in Fig. 2, where our results agree with the (not-shown) analytic  $\sigma_I$  function [34]. Fig. 2 also

FIG. 2: Rayleigh and photoionization scattering cross-sections for photon-hydrogen scattering (in units of  $\sigma_T$ ). The  $\sigma_e$  and  $\sigma_I$  are shown as a function of incident photon energy  $\omega$  in atomic units (ie. up to  $\approx 27$  eV). Our  $\sigma_e$  results agree with the analytic results of Gavrilu [32], with some discrepancy against the (as digitized by us) numerical results of Bergstrom *et al.* [8]. The FFAST  $\sigma_I$  results lie a few percent below ours [13].



shows physical resonances and that  $\sigma_e(\omega \rightarrow \infty) \approx \sigma_T$  in the non-relativistic limit. The Rayleigh scattering cross-sections between  $\omega = 0.37 - 0.55$  a.u., and up to  $\omega = 100$  a.u., are given in Supplemental Figs. 1 and 3.

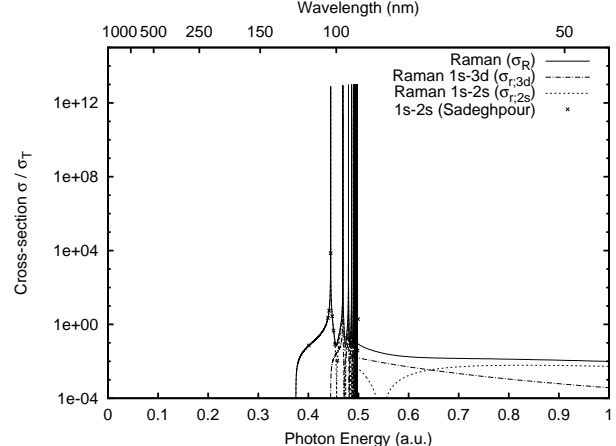
For (inelastic) Raman scattering to (physical) state  $j$

$$\sigma_{r;j}(\omega) = \sigma_T \omega (\omega'_j)^3 \left| \text{Re}[\alpha_{ij}(\omega)] + i \text{Im}_0[\alpha_{ij}(\omega)] \right|^2, \quad (4)$$

with spontaneously emitted photon frequency  $\omega'_j = \omega - \omega_{ij}$ . Thus the total Raman cross-section for an atom in an initial state  $i$  is  $\sigma_R(\omega) = \sum_{(j; E_j < \Delta)} \sigma_{r;j}(\omega)$  (see supplemental material for our basis-set-based choice of ionization location  $E = \Delta$ , which effectively demarcates the bound states from the pseudostates). Our Raman codes were able to be validated at energies below ionisation  $\omega < 0.5$  a.u., where previous photon-hydrogen Raman calculations have computed  $\text{H}(1s) \rightarrow \text{H}(2s)$  scattering [33], and excited initial state  $\text{H}(3s) \rightarrow \text{H}(3d)$  ‘Rayleigh’ scattering [35]. Our  $\text{H}(1s) \rightarrow \text{H}(2s)$ ,  $\text{H}(1s) \rightarrow \text{H}(3d)$ , and total Raman cross-sections are shown in Fig. 3. The individual  $\text{H}(1s) \rightarrow \text{H}(ns)$  Raman cross-sections above threshold rapidly vanish and revive as each of their matrix elements pass through a different ‘tune-out’ wavelength where  $|\alpha_{ij}(\omega)| \approx 0$ . The  $\text{H}(1s) \rightarrow \text{H}(nd)$  cross-sections are monotonically decreasing above threshold. The total Raman cross-section above  $\omega = 0.5$  a.u. monotonically decreases such that  $\sigma_R(\omega) \rightarrow 0$  as  $\omega \rightarrow \infty$  (see Supplemental Figs. 2 and 4 for cross-sections for  $\omega = 0.37 - 0.55$  a.u., and up to  $\omega = 100$  a.u.).

The final process considered here is that of Compton scattering, which opens up for frequencies above threshold  $\omega > |E_i|$ , and analytically requires the *differential* cross-section to be integrated over all possible outgoing

FIG. 3: Raman scattering cross-sections for photon-hydrogen scattering (in units of  $\sigma_T$ ). These are shown as a function of incident photon energy  $\omega$  in atomic units (ie. up to  $\approx 27$  eV). Our results are compared against the available ( $\omega < 0.5$ ) results for  $\text{H}(1s) \rightarrow \text{H}(2s)$  of Sadeghpour and Dalgarno [33]. The cross-section for  $\text{H}(1s) \rightarrow \text{H}(3d)$  is also shown. The sum of the individual cross-sections  $\sigma_R(\omega)$  is also shown as the solid line, and is seen to monotonically decrease.



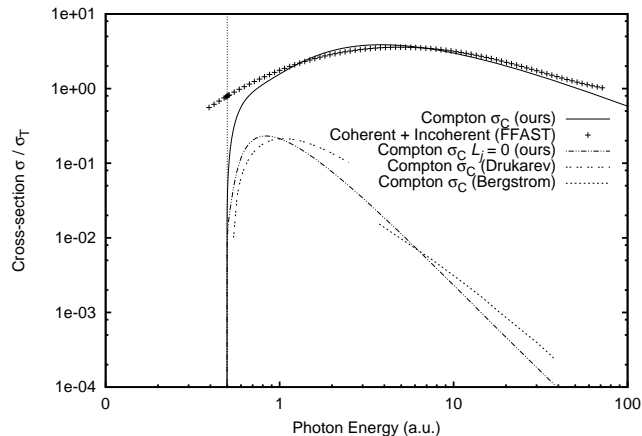
photon frequencies  $\omega'$  [12],

$$\sigma_C(\omega) = \int_{\omega'_{\min}}^{\omega'_{\max}} \frac{d\sigma_C}{d\omega} \Big|_{\omega'} d\omega' \approx \sum_{(j; E_j > \Delta)} \sigma_{r;j}(\omega), \quad (5)$$

where the largest emitted photon frequency  $\omega'_{\max} = \omega - |E_i|$ , whilst the smallest  $\omega'_{\min} = 0$ . The infra-red problem is that  $\frac{d\sigma_C}{d\omega}$  diverges as  $\omega' \rightarrow 0$ , resulting in an infinite cross-section, and thus previous analytic calculations of Bergstrom *et al.* [8] assumed  $\omega'_{\min} = 10$  eV, whilst Drukarev *et al.* [12] assumed  $\omega'_{\min} = 1$  eV. We, instead, adopt the approximation in Eqn. 5, adapting the same formulae from the Raman case since the finite set of pseudostates gives us a discrete sum. Note that our Raman vs Compton delineation is in the same spirit of previous work on excitation Raman vs ionization Raman photon-helium scattering [36]. The convergence of the sum towards the integral can be understood by considering that, as the basis size  $N_\ell$  is increased, more pseudostates are included and the magnitude of the individual cross-sections  $\sigma_{r;j}(\omega)$  decreases, whilst the  $\sigma_C(\omega)$  tends to remain constant (see Supplemental Fig. 5).

Our results for Compton scattering are shown in Fig. 4 where our results completely disagree by over three orders-of-magnitude with the previous results of Bergstrom *et al.* [8] and Drukarev *et al.* [12]. We, however, ran our calculations by including only the states with final  $L_j = 0$ , ie. ignoring the  $L_j = 2$  contributions which turn out to dominate the sum in Eqn. 5. In doing so we find qualitative agreement of our  $0 \rightarrow 1 \rightarrow 0$  cross-section with these previous calculations, which relied on numerical truncation of analytic differential cross-sections. Our total results instead broadly agree with

FIG. 4: Comparisons of Compton scattering cross-sections up to high energies for photon-hydrogen scattering (in units of  $\sigma_T$ ). The summed  $\sigma_C(\omega)$  is shown as a function of incident photon energy  $\omega$  in atomic units (ie. up to  $\approx 2700$  eV). The summed cross-section is also shown when only the  $L_j = 0$  contributions are included, which approximately agrees with the results of Bergstrom *et al.* [8] and Drukarev *et al.* [12] (their results were digitized by us). The FFAST results are also shown [13].



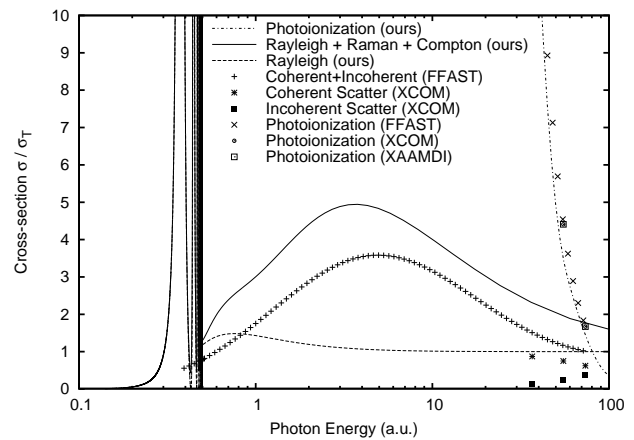
the FFAST coherent + incoherent results [13]. Coherent scattering generally refers to elastic (Rayleigh) scattering, whilst incoherent scattering means inelastic (Compton) scattering [15].

*Total Cross-section* — The total cross-section summing all Rayleigh, Raman, Compton processes is shown in Fig. 5, showing qualitative agreement with the FFAST data. The NIST-based XCOM and XAAMDI database results are presented in Fig. 5 [37–40]. The photoionization cross-section only appears in Fig. 5 towards keV energies where it drops down in magnitude to be below the others. Our data shows that Wentzel’s rule [41] is never applicable to hydrogen, that is, the sum over the elastic and inelastic total cross-sections does not tend to that of a free electron (ie. the Thomson cross-section) over the energy range before higher-order effects take over [8].

*Conclusion* — We have introduced a computational method for computing various cross-sections of photon-atom scattering for any initial state from a single atomic structure calculation. We find the expected behaviour of the Compton scattering towards low-energies and our calculations do not appear to suffer from the infrared catastrophe. Effectively a computational atom-in-box sets a maximum wavelength that can be ‘mea-

sured’ [10, 42]. Our results are able to reach up to energies where the beyond-dipole-approximation and relativistic/retardation effects become important and thus provide a benchmark for future work. Our methods can be extended to compute the cross-sections for atoms in various initial states, and where knowledge of the possible scattering processes will help guide experimentalists when designing atomic and molecular experiments.

FIG. 5: Comparisons of scattering cross-sections up to high energies for photon-hydrogen scattering (in units of  $\sigma_T$ ). These are shown as a function of incident photon energy  $\omega$  in atomic units (ie. up to  $\approx 2700$  eV). The coherent, incoherent, and photoionization data from FFAST [13] and XCOM [39] is shown, as well as photoionization from XAAMDI [40]. Note that the  $y$ -axis is here shown not on logscale.



In particular, it will be worthwhile to compute Rayleigh, Raman, and Compton scattering cross-sections for multi-electron atoms where Cooper minima in the photoionization cross-sections and resonances can occur [15].

## Acknowledgments

The work of MWJB was supported by an Australian Research Council Future Fellowship (FT100100905). YC was supported by the National Natural Science Foundation of China (Grant No. 11304063). The work of YC was also partially enabled by a Discovery Project (DP-1092620) of Prof. Jim Mitroy (deceased). We thank Dr. Julian Berengut, A/Prof. Tom Stace, and Prof. Dave Kielpinski for useful conversations and Dr. Sergey Novikov for correspondence about matrix elements.

- [1] J. J. Sakurai, *Advanced Quantum Mechanics* (Addison-Wesley, 1967).
- [2] W. Heitler, *The Quantum Theory of Radiation* (Clarendon Press, Oxford, 1954), (Third Edition).
- [3] N. B. Delone and V. P. Krainov, *Multiphoton processes in*

*atoms* (Springer-Verlag, Berlin Heidelberg, 2000), URL <http://dx.doi.org/10.1007/978-3-642-57208-1>.

- [4] D. G. Fried, T. C. Killian, L. Willmann, D. Landhuis, S. C. Moss, D. Kleppner, and T. J. Greytak, *Phys. Rev. Lett.* **81**, 3811 (1998), URL

- <http://dx.doi.org/10.1103/PhysRevLett.81.3811>.
- [5] G. A. Kyrala and T. D. Nichols, Phys. Rev. A **44**, R1450 (1991).
- [6] D. Kielpinski, R. T. Sang, and I. V. Litvinyuk, J. Phys. B **47**, 204003 (2014).
- [7] A. Delserieys, F. Y. Khattak, S. Sahoo, G. F. Gribakin, C. L. S. Lewis, and D. Riley, Phys. Rev. A **78**, 055404 (2008).
- [8] P. M. Bergstrom, T. Surić, K. Pisk, and R. H. Pratt, Phys. Rev. A **48**, 1134 (1993), URL <http://link.aps.org/doi/10.1103/PhysRevA.48.1134>.
- [9] M. Gavrilă, Lettere al Nuovo Cimento **2**, 180 (1969), URL <http://dx.doi.org/10.1007/BF02755741>.
- [10] M. Gavrilă, Phys. Rev. A **6**, 1348 (1972), URL <http://dx.doi.org/10.1103/PhysRevA.6.1348>.
- [11] M. Gavrilă, Revue Roumaine de Physique **19**, 473 (1974).
- [12] E. G. Drukarev, A. I. Mikhailov, and I. A. Mikhailov, Phys. Rev. A **82**, 023404 (2010), URL <http://dx.doi.org/10.1103/PhysRevA.82.023404>.
- [13] C. T. Chantler, J. Phys. Chem. Ref. Data **24**, 71 (1995), URL <http://dx.doi.org/10.1063/1.555974>.
- [14] R. H. Pratt, Rad. Phys. Chem. **70**, 595 (2004), URL <http://dx.doi.org/10.1016/j.radphyschem.2003.12.032>.
- [15] R. H. Pratt, Rad. Phys. Chem. **95**, 4 (2014), URL <http://dx.doi.org/10.1016/j.radphyschem.2013.10.018>.
- [16] J. Mitroy, J. Y. Zhang, M. W. J. Bromley, and S. I. Young, Phys. Rev. A **78**, 012715 (2008), URL <http://dx.doi.org/10.1103/PhysRevA.78.012715>.
- [17] J. Mitroy, M. S. Safronova, and C. W. Clark, J. Phys. B **43**, 202001 (2010), URL <http://dx.doi.org/10.1088/0953-4075/43/20/202001>.
- [18] L. Y. Tang, M. W. J. Bromley, Z. C. Yan, and J. Mitroy, Phys. Rev. A **87**, 032507 (2013), URL <http://dx.doi.org/10.1103/PhysRevA.87.032507>.
- [19] J. Jiang, J. Mitroy, Y. Cheng, and M. W. J. Bromley, At. Data Nucl. Data Tables **101**, 158 (2015), URL <http://www.sciencedirect.com/science/article/pii/S0092640114000722>.
- [20] J. Mitroy and M. W. J. Bromley, Phys. Rev. Lett. **98**, 173001 (2007), URL <http://dx.doi.org/10.1103/PhysRevLett.98.173001>.
- [21] P. W. Langhoff and M. Karplus, J. Chem. Phys. **52**, 1435 (1970).
- [22] P. W. Langhoff, Chem. Phys. Lett. **22**, 60 (1973).
- [23] P. W. Langhoff and C. T. Corcoran, J. Chem. Phys. **61**, 146 (1974).
- [24] P. W. Langhoff, J. Sims, and C. T. Corcoran, Phys. Rev. A **10**, 829 (1974).
- [25] P. W. Langhoff, C. T. Corcoran, J. S. Sims, F. Weinhold, and R. M. Glover, Phys. Rev. A **14**, 1042 (1976), URL <http://dx.doi.org/10.1103/PhysRevA.14.1042>.
- [26] P. Eisenberger and P. M. Platzman, Phys. Rev. A **2**, 415 (1970), URL <http://dx.doi.org/10.1103/PhysRevA.2.415>.
- [27] V. Chandrasekharan and B. Silvi, J. Phys. B **14**, 4327 (1981), URL <http://stacks.iop.org/0022-3700/14/i=22/a=016>.
- [28] K. D. Bonin and V. V. Kresin, *Electric-dipole polarizabilities of atoms, molecules and clusters* (World Scientific, River Edge, NJ, Singapore, 1997), URL <http://www.worldscientific.com/worldscibooks/10.1142/2962>.
- [29] F. Le Kien, P. Schneeweiss, and A. Rauschenbeutel, Eur. Phys. J. D **67**, 92 (2013).
- [30] M. Lepers, J. F. Wyart, and O. Dulieu, Phys. Rev. A **89**, 022505 (2014).
- [31] C. M. J. Wijers, Phys. Rev. A **70**, 063807 (2004).
- [32] M. Gavrilă, Phys. Rev. **163**, 147 (1967), URL <http://link.aps.org/doi/10.1103/PhysRev.163.147>.
- [33] H. R. Sadeghpour and A. Dalgarno, J. Phys. B **25**, 4801 (1992), URL <http://stacks.iop.org/0953-4075/25/i=22/a=015>.
- [34] I. I. Sobelman, *Atomic Spectra and Radiative Transitions* (Springer, Berlin, 1996), (corrected Second Edition 1996), URL <http://link.springer.com/book/10.1007%2F978-3-642-76907-8>.
- [35] V. Florescu and A. Cionga, Z. Phys. A **321**, 187 (1985), URL <http://dx.doi.org/10.1007/BF01493437>.
- [36] T. Grosjes, B. Piraux, and R. Shake-shaft, Phys. Rev. A **59**, 3088 (1999), URL <http://link.aps.org/doi/10.1103/PhysRevA.59.3088>.
- [37] J. H. Hubbell, W. J. Veigele, E. A. Briggs, R. T. Brown, D. T. Cromer, and R. J. Hower-ton, J. Phys. Chem. Ref. Data **4**, 471 (1975), URL <http://dx.doi.org/10.1063/1.555523>.
- [38] J. H. Hubbell and I. Overbo, J. Phys. Chem. Ref. Data **8**, 69 (1979), URL <http://dx.doi.org/10.1063/1.555593>.
- [39] J. H. Hubbell, S. Seltzer, J. Chang, J. Coursey, R. Sukumar, D. Zucker, and K. Olsen, *XCOM: Photon Cross Section Database (version 1.5)* (2010), URL <http://physics.nist.gov/xcom>.
- [40] J. H. Hubbell and S. M. Seltzer, *Tables of x-ray mass attenuation coefficients and mass energy-absorption coefficients (version 1.4)* (2004), URL <http://physics.nist.gov/xaamdi>.
- [41] I. G. Kaplan and G. L. Yudin, Sov. Phys. JETP **42**, 4 (1976), zh. Eksp. Teor. Fiz. **69**, 9 (1975).
- [42] M. Gavrilă, Phys. Rev. A **6**, 1360 (1972), URL <http://dx.doi.org/10.1103/PhysRevA.6.1360>.

# Supplemental data — The photon scattering cross-sections of atomic hydrogen

Swaantje J. Grunefeld and Michael W. J. Bromley\*

*School of Mathematics and Physics, The University of Queensland, Brisbane, St Lucia, QLD 4072, Australia*

Yongjun Cheng

*Academy of Fundamental and Interdisciplinary Science,  
Harbin Institute of Technology, Harbin 150080, PR China and  
School of Engineering, Charles Darwin University, Darwin NT 0909, Australia*

(Dated: June 6, 2016)

We present: in section (I) some formulae underlying our computations, wherein we extend the treatment by Delsierieys *et al.* [1] to handle the above threshold region, in section (II) discussion of how we determine which states are bound and which are treated as pseudostates, and finally in section (III) some zoomed in plots spanning the physical resonance area, and in section (IV) some demonstrations of the convergence of our photon-hydrogen scattering cross-sections with respect to the Laguerre basis employed here.

PACS numbers: 31.15.ap, 32.30.-r, 32.80.Fb

## I. FORMULAE

Our atom-in-a-box calculation generates a large number of transition matrix elements. These connect the  $N_\ell$  number of Laguerre basis functions for each partial wave to each other through dipole allowed reduced matrix elements of operator  $\hat{z} \equiv rC^1(\hat{r})$ , that are independent of the magnetic quantum number. Given  $C^1(\hat{r})$  is the spherical tensor of rank-1, for eigenstate  $i$  and eigenstate  $j$ , the reduced matrix elements are

$$\begin{aligned} \langle j || rC^1(\hat{r}) || i \rangle &= \int \int Y_{\ell_j}(\theta, \phi) C^1(\theta, \phi) Y_{\ell_i}(\theta, \phi) \sin \theta d\theta d\phi \int \psi_j(r) r \psi_i(r) r^2 dr \\ &= (-1)^{\ell_j} \sqrt{(2\ell_j + 1)(2\ell_i + 1)} \begin{pmatrix} \ell_j & 1 & \ell_i \\ 0 & 0 & 0 \end{pmatrix} \int \psi_j(r) r \psi_i(r) r^2 dr. \end{aligned} \quad (1)$$

The orthogonal Laguerre basis functions that we choose to use all have the same long-range parameterisation,  $\exp(-\lambda_\ell r)$ , for each partial-wave,  $\ell$ . By providing a set of basis functions with fixed  $\lambda = 0.5$ , they are explicitly not a set of eigenstates of hydrogen (as hydrogen eigenstates have  $\lambda_n = \frac{1}{2}n$  [2]). Thus we generate a set of low-lying bound states as well as a (reasonably well-defined) set of higher-lying Rydberg states, along with a set of ( $E > 0$ ) pseudostates that reflect the finite nature of the effective box induced by having a finite number of basis functions.

In our code the radial integrals are performed numerically [3], which has allowed us in the past to perform numerous calculations of one- and two-electron atoms including mixtures of Laguerre and Slater Type Orbitals to represent frozen Hartree-Fock-based core electrons [3, 4]. Here we use a large radius grid spanning to maximum of  $\approx 1000$  a.u. using 4096 grid points with 16-point Gauss-Legendre radial integration quadrature [3].

The ‘Kramers-Heisenberg’ matrix element is determined here as a transition polarizability between some initial state  $|i; L_i S\rangle$  and final state  $|j; L_j S\rangle$  through a complete set of intermediate states  $|t; L_t S\rangle$ . In terms of sums over reduced matrix elements with  $LS$ -coupled wavefunctions and assuming linear photon polarization [1],

$$\begin{aligned} \alpha_{ji}(\omega) &= \sum_t C_{L_i, L_t, L_j} \left[ \frac{\langle j || z || t \rangle \langle t || z || i \rangle}{\varepsilon_{ti} - \omega - i\frac{1}{2}\Gamma_{ti}(\omega)} \right] + \sum_t C_{L_i, L_t, L_j} \left[ \frac{\langle j || z || t \rangle \langle t || z || i \rangle}{\varepsilon_{tj} - (-\omega) - i\frac{1}{2}\Gamma_{tj}(\omega)} \right] \\ &+ \int_0^\infty \frac{C_{L_i, L_\epsilon, L_j}}{\rho(\epsilon)} \left[ \frac{\langle j || z || \epsilon \rangle \langle \epsilon || z || i \rangle}{\varepsilon_{\epsilon i}} \right] d\epsilon + \int_0^\infty \frac{C_{L_i, L_\epsilon, L_j}}{\rho(\epsilon)} \left[ \frac{\langle j || z || \epsilon \rangle \langle \epsilon || z || i \rangle}{\varepsilon_{\epsilon j} - (-\omega)} \right] d\epsilon, \end{aligned} \quad (2)$$

where, in atomic units,  $\varepsilon_{ab} = E_b - E_a$ . The bound eigenstates, denoted by  $t$ , form an infinite set. As the sums have bound intermediate states with physical linewidths, the decay rates  $\Gamma_{ti}$  or  $\Gamma_{tj}$  are included. The integrals describe the

---

\*Electronic address: brom@physics.uq.edu.au

transitions where the intermediate states are continuum states, denoted by energy  $\epsilon$ . The transition matrix elements in the continuum integrals are normalized by the energy density  $\rho(\epsilon)$  of the continuum states. The terms with  $-\omega$  in the denominator indicate photon absorption followed by emission. The terms with  $-(-\omega)$  in the denominator indicate photon emission followed by absorption. For the H(1s) initial state considered here,  $C_{0,1,0} = \frac{1}{3}$  and also  $C_{0,1,2} = \frac{1}{3}$ , where we only have intermediate  $L_\epsilon = L_t = 1$ . Whilst Eqn. (2) is for the Raman case, it covers the Rayleigh case where  $j = i$ .

Here we break up the terms into the bound and continuum contributions. We sum up the bound states using the notation  $T_{ba} = \langle b||z||a \rangle$ , as

$$\text{Re}_0(\alpha_{ji}(\omega)) + i\text{Im}_0(\alpha_{ji}(\omega)) \approx \sum_{b=1}^{N_b} C_{L_i, L_b, L_j} \left[ \frac{T_{jb}T_{bi}}{\varepsilon_{bi} - \omega - i\frac{1}{2}\Gamma_{bi}(\omega)} + \frac{T_{jb}T_{bi}}{\varepsilon_{bj} - (-\omega) - i\frac{1}{2}\Gamma_{bj}(\omega)} \right], \quad (3)$$

where  $N_b$  is the finite number of (intermediate) bound states in a given calculation.

Next we consider the first continuum integral in Eqn. (2), both below and above ionization threshold. For the first continuum integral in Eqn. (2), when  $\omega$  lies below the ionization threshold,

$$\text{Re}_1(\alpha_{ji}(\omega)) = \int_0^\infty \frac{C_{L_i, L_\epsilon, L_j}}{\rho(\epsilon)} \left[ \frac{T_{j\epsilon}T_{\epsilon i}}{\varepsilon_{\epsilon i} - \omega} \right] d\epsilon \approx \sum_{p=1}^{N_p} \frac{C_{L_i, L_p, L_j}}{\Delta\varepsilon_p} \left[ \frac{T_{jp}T_{pi}}{\varepsilon_{pi} - \omega} \right] \Delta\varepsilon_p, \quad (4)$$

where  $\rho(\epsilon) \approx \Delta\varepsilon_p$ . Note that the sum over the pseudostates is only an approximation to the integral, however, the sum tends to monotonically converge as the basis set increases. When  $\omega$  lies above the ionization threshold, unphysical poles occur at  $\omega = \varepsilon_{\epsilon i}$ . We have to integrate around the pole by introducing a small complex term into the frequency  $z = \omega + i0^+$  where the  $+$  indicates approaching zero from above. This means that we apply the Cauchy principal theorem,

$$\text{Re}_1(\alpha_{ji}(z)) - i\text{Im}_1(\alpha_{ji}(z)) = \int_0^\infty \frac{\mathcal{F}(\epsilon)}{\varepsilon_{\epsilon i} - \omega - i0^+} d\epsilon \equiv \mathcal{P} \int_0^\infty \frac{\mathcal{F}(\epsilon)}{\varepsilon_{\epsilon i} - \omega} d\epsilon - i\pi \mathcal{F}(\epsilon) \Big|_{\epsilon=\omega+E_i}, \quad (5)$$

where  $\mathcal{F}(\epsilon) = C_{L_i, L_\epsilon, L_j} T_{j\epsilon} T_{\epsilon i} / \rho(\epsilon)$ . Again, however, we have a discrete set of pseudostates. Thus we evaluate the above threshold values **only** at discrete frequencies  $\omega_{ni} = E_n - E_i$ , which correspond to the frequencies required to resonantly excite the pseudostates, and we remove the single singular term from the sum:

$$\text{Re}_1(\alpha_{ji}(\omega_{ni})) - i\text{Im}_1(\alpha_{ji}(\omega_{ni})) \approx \left( \sum_{p \neq n}^{N_p} \frac{C_{L_i, L_p, L_j}}{\Delta\varepsilon_p} \left[ \frac{T_{jp}T_{pi}}{\varepsilon_{pi} - \omega_{ni}} \right] \Delta\varepsilon_p \right) - i\pi C_{L_i, L_n, L_j} \frac{T_{jn}T_{ni}}{\frac{1}{2}(E_{(n+1)} - E_{(n-1)})}, \quad (6)$$

with modification of the finite differencing when computing at the first  $n = 1$  or the last  $n = N_p$  pseudostates.

The second continuum integral in Eqn. (2), corresponds first to photon emission, followed by absorption and thus has no such pole due to the continuum. This integral can be evaluated both above and below threshold at any incident photon energy as

$$\text{Re}_2(\alpha_{ji}(\omega)) = \int_0^\infty \frac{C_{L_i, L_\epsilon, L_j}}{\rho(\epsilon)} \left[ \frac{\langle j||z||\epsilon \rangle \langle \epsilon||z||i \rangle}{\varepsilon_{\epsilon j} - (-\omega)} \right] d\epsilon \approx \sum_{p=1}^{N_p} \frac{C_{L_i, L_p, L_j}}{\Delta\varepsilon_p} \left[ \frac{T_{jp}T_{pi}}{\omega_{pj} + \omega} \right] \Delta\varepsilon_p. \quad (7)$$

This term only contains a divergence for the case of resonant ‘anti-Stokes’ Raman processes, where the final state lies at an energy below the initial state, which are not considered here.

Thus for either Rayleigh ( $i = j$ ) or Raman ( $i \neq j$ , where  $j \in [1, N_b]$ ) we can compute the transition polarizability at any frequency  $\omega$  below threshold:

$$\alpha_{ji}(\omega) = \text{Re}_0(\alpha_{ji}(\omega)) + \text{Re}_1(\alpha_{ji}(\omega)) + \text{Re}_2(\alpha_{ji}(\omega)) + i\text{Im}_0(\alpha_{ji}(\omega)), \quad (8)$$

whilst for  $\omega$  above threshold, we evaluate at the discrete pseudostate frequencies

$$\alpha_{ji}(\omega_{ni}) = [\text{Re}_0(\alpha_{ji}(\omega_{ni})) + \text{Re}_1(\alpha_{ji}(\omega_{ni})) + \text{Re}_2(\alpha_{ji}(\omega_{ni}))] + i\text{Im}_0(\alpha_{ji}(\omega_{ni})) - i\text{Im}_1(\alpha_{ji}(\omega_{ni})). \quad (9)$$

For the case of Compton scattering, which is only available when the final state lies in the continuum (ie.  $j \rightarrow \epsilon_j$ ), it can only be computed when the incident photon frequency is  $\omega \geq \varepsilon_{ji}$ . However, we simply apply all of the same pseudostate machinery as outlined above when computing these transition polarizabilities. That is, we compute the integrals by assuming that both the intermediate states and final states are discrete pseudostates and evaluate these at the discretized frequencies  $\omega_{ni} = E_n - E_i$ , where  $n$  is the intermediate  $L = 1$  pseudostate.

## II. CHOICE OF WHICH EIGENSTATES ARE BOUND VS PSEUDOSTATES

Since we are computing the non-relativistic hydrogen atom, with the basis set employed here we obtain  $E_{1s} = -0.5$  a.u. to near machine precision. The natural ionization potential is then located exactly at  $E = 0$ . Table I shows the transition data from the H(1s) state to the lowest 25  $p$ -states from the largest  $N = 120$  calculation. This table shows that in a single-shot Laguerre calculation we are able to accurately reproduce up to approximately the  $n = 15$  Rydberg state. Looking at the oscillator strength pattern, it reaches a minimum for the  $n = 15$  state, after which the oscillator strengths start increasing again. Not shown is that they reach another maximum at the 85-th  $\ell = 1$  eigenstate ( $E_{86p} = 0.409641$  a.u., with  $f_{if} = 0.007975$ ), before dropping down towards zero. This corresponds to photon frequencies of  $\omega \approx 0.9$  a.u., which is approximately where the (above threshold) Rayleigh and Compton scattering peaks occur.

TABLE I: The  $1s - np$  transition data for the first 25  $\ell = 1$  eigenstates from our  $N = 120$  Laguerre basis set calculation, whose results are compared to the exact Rydberg values. The  $n_i \rightarrow n_f$  column indicates the initial to final state transition. The  $E_f$  (calc) column gives the eigenenergies in atomic units of the final state from the calculation, whilst  $E_f$  (exact) column gives the exact energies based on the Rydberg formula ( $E_n = -0.5/n^2$ ). The transition oscillator strengths  $f_{if}$  (calc) are from the calculation, whilst the  $f_{if}$  (exact) are from the analytic formulae [5]. The final column gives the relative difference between the oscillator strengths ( $= (f_{if}(\text{calc}) - f_{if}(\text{exact}))/f_{if}(\text{exact})$ ). Two row demarcations are given, the first to indicate where the  $E < 0$  bound states have a minima in the oscillator strengths and start to lose accuracy, the second where the  $E > 0$  pseudostates begin.

$n_i \rightarrow n_f$	$E_f$ (calc)	$E_f$ (exact)	$f_{if}$ (calc)	$f_{if}$ (exact)	(rel. diff.)
$1s \rightarrow 2p$	-0.125000	-0.125000	0.416197	0.416197	0.000000
$1s \rightarrow 3p$	-0.055556	-0.055556	0.079102	0.079102	0.000000
$1s \rightarrow 4p$	-0.031250	-0.031250	0.028991	0.028991	0.000000
$1s \rightarrow 5p$	-0.020000	-0.020000	0.013938	0.013938	0.000000
$1s \rightarrow 6p$	-0.013889	-0.013889	0.007799	0.007799	0.000000
$1s \rightarrow 7p$	-0.010204	-0.010204	0.004814	0.004814	0.000000
$1s \rightarrow 8p$	-0.007813	-0.007813	0.003183	0.003183	0.000000
$1s \rightarrow 9p$	-0.006173	-0.006173	0.002216	0.002216	0.000000
$1s \rightarrow 10p$	-0.005000	-0.005000	0.001605	0.001605	0.000000
$1s \rightarrow 11p$	-0.004132	-0.004132	0.001201	0.001201	0.000000
$1s \rightarrow 12p$	-0.003472	-0.003472	0.000921	0.000921	0.000000
$1s \rightarrow 13p$	-0.002959	-0.002959	0.000723	0.000723	0.000076
$1s \rightarrow 14p$	-0.002550	-0.002551	0.000582	0.000577	0.007629
$1s \rightarrow 15p$	-0.002206	-0.002222	0.000531	0.000469	0.132738
$1s \rightarrow 16p$	-0.001850	-0.001953	0.000609	0.000386	0.578355
$1s \rightarrow 17p$	-0.001428	-0.001730	0.000723	0.000321	1.253279
$1s \rightarrow 18p$	-0.000933	-0.001543	0.000831	0.000270	2.073712
$1s \rightarrow 19p$	-0.000372	-0.001385	0.000930	0.000230	3.050423
$1s \rightarrow 20p$	0.000254	-	0.001024	-	-
$1s \rightarrow 21p$	0.000940	-	0.001116	-	-
$1s \rightarrow 22p$	0.001688	-	0.001205	-	-
$1s \rightarrow 23p$	0.002496	-	0.001293	-	-
$1s \rightarrow 24p$	0.003365	-	0.001381	-	-
$1s \rightarrow 25p$	0.004295	-	0.001468	-	-
$1s \rightarrow 26p$	0.005287	-	0.001555	-	-

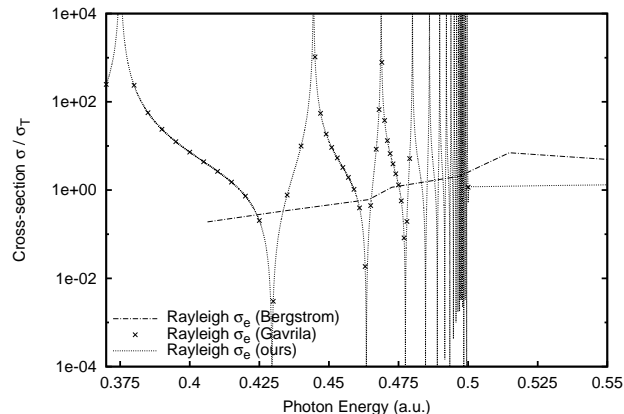
We were able to use Table I to demarcate where the bound states end and where the pseudostates begin. We choose this energy to be just above where the oscillator strength reaches a minima. For the present  $N_\ell = 120$  calculations this is at  $\Delta_{120} \approx (-0.002206 + -0.001850)/2 = -0.002028$  a.u.. The Raman final states are thus those with  $E_n < -0.00203$ , whereas the Compton have  $E_n > -0.00203$ . This choice, rather than the exact  $\Delta = 0$ , means that our effective ionization potential in our box has a small residual error in it. However, the moving of the states with  $\Delta_{N_\ell} < E_n < 0$  to be counted as Compton rather than Raman removes spurious cross-sections that were polluting the convergence of the total Raman cross-section at photon-frequencies above threshold. Essentially, the wavefunctions corresponding to the  $16p$  to  $19p$  states appear to contain a significant mixture of both Rydberg and continuum information. This does mean that the  $Im_1$  contribution also starts at similarly lower photon energy  $0.5 - 0.00203 = 0.4979$  a.u., and it does mean that our calculations have a large error in this relatively small energy range around threshold.



### III. A ZOOMED IN VIEW OF THE CROSS-SECTIONS

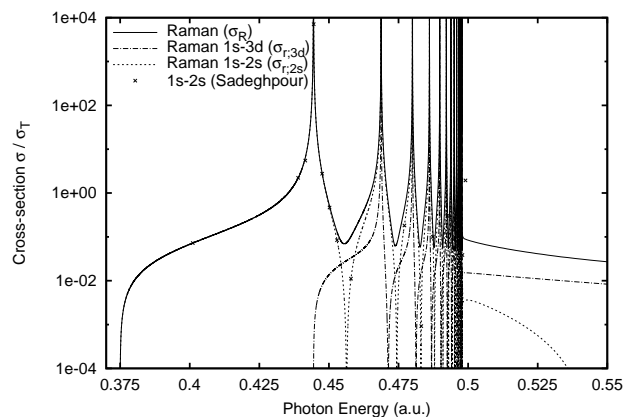
Fig. 1 shows the Rayleigh cross-section between frequencies  $0.37 - 0.55$  a.u., which spans the atomic (physical) resonances and also up into the continuum. Fig. 2 shows the Raman cross-section across the same frequency range.

FIG. 1: Rayleigh scattering cross-sections for photon-hydrogen scattering (in units of  $\sigma_T$ ). The  $\sigma_e$  are shown as a function of incident photon energy  $\omega$  in atomic units. Our  $\sigma_e$  results agree with the analytic results of Gavrilu [6], with some discrepancy against the (as digitized by us) numerical results of Bergstrom *et al.* [7].



This gives a closer look at the behaviour of the Raman cross-section near threshold. Table II gives three data points for

FIG. 2: Raman scattering cross-sections for photon-hydrogen scattering (in units of  $\sigma_T$ ). These are shown as a function of incident photon energy  $\omega$  in atomic units. Our results are shown and compared against the (below threshold only) results for  $H(1s) \rightarrow H(2s)$  of Sadeghpour and Dalgarno [8]. The cross-section for  $H(1s) \rightarrow H(3d)$  is also shown.



Rayleigh and Raman cross-sections. The photoionization cross-section is also given for the frequency above threshold. Above threshold the cross-sections must be computed on a pseudostate energy. Therefore, the values at  $0.52$  a.u. were determined by interpolating linearly between two pseudostate frequencies. This introduces an uncertainty in the value, resulting in only few significant figures. Table II gives the cross-section at  $\omega = 0.52$  a.u. as calculated for three different basis sets to show the convergence. Both in Raman and Compton this shows that the convergence is not monotonic with respect to the number of Laguerres in the basis set, and will be examined in future work.

### IV. CONVERGENCE OF CROSS-SECTIONS WITH LAGUERRE-BASIS SIZE

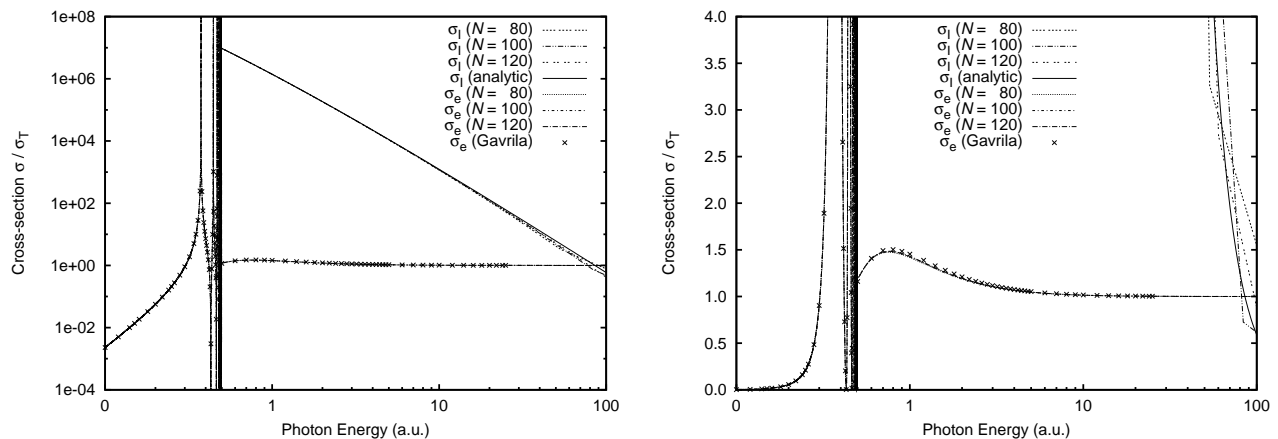
We ran off a series of calculations with the inclusion of various numbers of Laguerre functions,  $N_\ell$  for each partial-wave. The convergence of the Rayleigh and photoionization scattering cross-sections are shown in Fig. 3. Note that

TABLE II: The Rayleigh, Raman, Photoionization and Compton cross-sections (in units of  $\sigma_T$ ) are given for three frequencies. The cross-sections at frequency  $\omega = 0.52$  a.u. are presented for basis sets with  $N = 80$ ,  $N = 100$  and  $N = 120$  Laguerres for each partial wave.

$\omega$ (a.u.)	$N$	Rayleigh $\sigma_e/\sigma_T$	Raman $\sigma_R/\sigma_T$	Photoionisation $\sigma_I/\sigma_T$	Compton $\sigma_C/\sigma_T$
0.40	80	7.2448357561099925	0.0677208258644729		
0.40	100	7.2448357561099925	0.0677208258644729		
0.40	120	7.2448357561099925	0.0677208258644729		
0.45	80	12.769933387763700	0.5657804519972952		
0.45	100	12.769933387763700	0.5657804519972952		
0.45	120	12.769933387763700	0.5657804519972952		
0.52	80	1.244	0.0456	$8.531 \times 10^6$	0.1524
0.52	100	1.242	0.0462	$8.530 \times 10^6$	0.1517
0.52	120	1.240	0.0461	$8.528 \times 10^6$	0.1519

the highest three eigenenergies in the  $N = 120$  calculation are  $E_{119p} = 59.7669$ ,  $E_{120p} = 119.823$ ,  $E_{121p} = 357.323$  a.u., and thus it is no surprise that the polarizabilities develop observable kinks around the  $\omega \approx 100$  a.u. range.

FIG. 3: Convergence of Rayleigh and photoionization scattering cross-sections for photon-hydrogen scattering (in units of  $\sigma_T$ ). The  $\sigma_e$  and  $\sigma_I$  are shown as a function of incident photon energy  $\omega$  in atomic units (ie. up to  $\approx 2700$  eV) for various Laguerre-basis set sizes  $N$ . Our results broadly agree with previous (purely analytic) results as shown. Two plots are given to show the behaviour of Rayleigh and photoionization (left) as well as to highlight the small peak in the Rayleigh cross-section (right) by plotting on a smaller linear scale.



The convergence of the Raman scattering cross-sections are shown for the total  $\sigma_R(\omega) = \sum_{(j; E_j < \Delta_N)} \sigma_{R;j}(\omega)$  for various  $N_\ell$  (left) and the summed cross-section when only the  $L_j = 0$  or  $L_j = 2$  contributions are included (right). Fig. 4 shows that the  $L_j = 0$  contribution rapidly declines just above threshold, and then increases rapidly. The  $L_j = 2$  contribution exhibits a small peak which changes with basis set size. This uncertainty in the (relatively small) cross-section will be studied further in future work.

The convergence of the Compton scattering cross-sections are shown (in Fig. 5) when only the  $L_j = 0$  or  $L_j = 2$  contributions are included for various  $N_\ell$ . Here we show, as per paper, that the  $L_j = 2$  contribution dominates the total Compton cross-section. Fig. 5 demonstrates that there is only a small change in the Compton cross-section when the size of the basis set is varied.

- 
- [1] A. Delsierieys, F. Y. Khattak, S. Sahoo, G. F. Gribakin, C. L. S. Lewis, and D. Riley, Phys. Rev. A **78**, 055404 (2008).
  - [2] M. W. J. Bromley and J. Mitroy, Phys. Rev. A **67**, 062709 (2003).
  - [3] M. W. J. Bromley and J. Mitroy, Phys. Rev. A **65**, 012505 (2001), URL <http://dx.doi.org/10.1103/PhysRevA.65.012505>.
  - [4] J. Mitroy and M. W. J. Bromley, Phys. Rev. A **68**, 035201 (2003).
  - [5] H. A. Bethe and E. E. Salpeter, *Quantum mechanics of one- and two-electron atoms* (Academic Press, New York, 1957).
  - [6] M. Gavril, Phys. Rev. **163**, 147 (1967), URL <http://link.aps.org/doi/10.1103/PhysRev.163.147>.

FIG. 4: Convergence of Raman scattering cross-sections for photon-hydrogen scattering (in units of  $\sigma_T$ ) for various Laguerre-basis set sizes  $N$ . These are shown as a function of incident photon energy  $\omega$  in atomic units (ie. up to  $\approx 2700$  eV). Our results are shown for the sum of the individual cross-sections  $\sigma_R(\omega)$  (left) and for the  $L_j = 0$  or  $L_j = 2$  contributions (right). The total cross-section (left) has a bi-modal decay above threshold due to the two different sets of contributions. Note also that there are residual issues with the convergence of the (relatively small) Raman cross-sections above threshold due to the small pollution of the highest-lying ‘bound’ state/s which have a small mixture of pseudostate character which should really be contributing to the (much larger) Compton cross-sections. This can be seen by comparing the frequency location of the two Raman peaks in the (right) plot against the location of the equivalent two Compton peaks in Fig. 5(right).

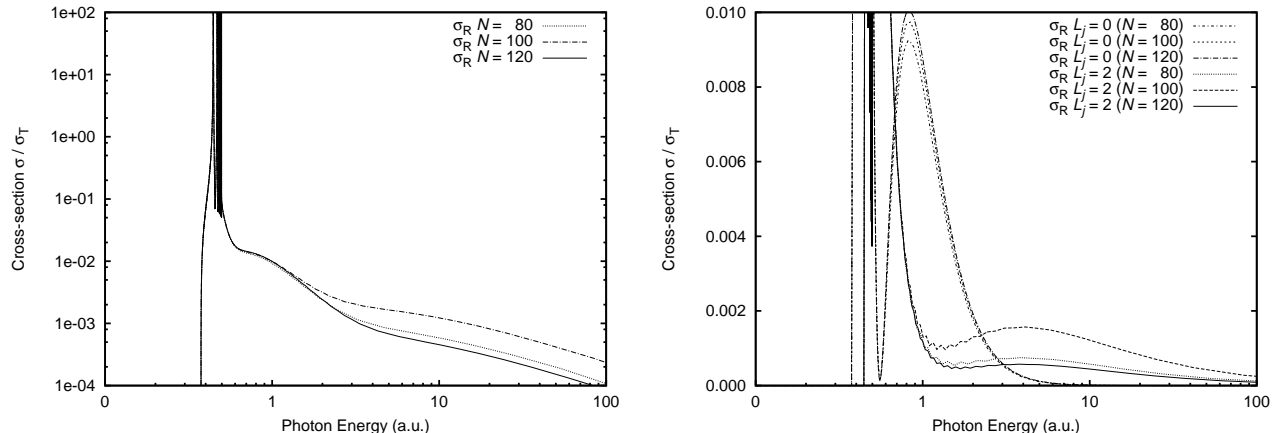
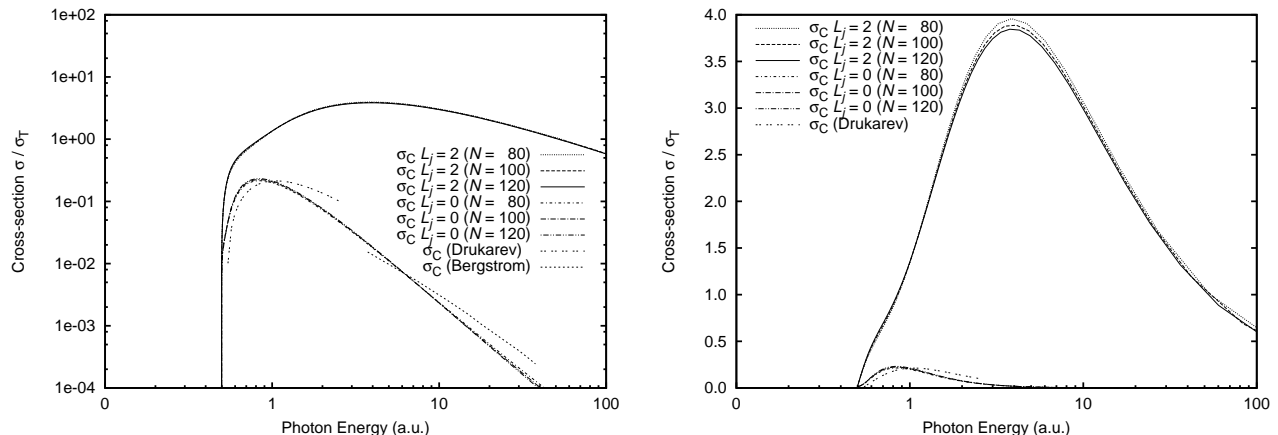


FIG. 5: Convergence of Compton scattering cross-sections for photon-hydrogen scattering (in units of  $\sigma_T$ ) for various Laguerre-basis set sizes  $N$ . The summed cross-section is shown when only the  $L_j = 0$  contributions are included, which approximately agrees with the results of Bergstrom *et al.* [7] and Drukarev *et al.* [9] which are also shown. The summed cross-section when only the  $L_j = 2$  contributions are included is also shown. The Compton cross-sections are plotted on a y-logscale (left) to show the behaviour of the  $L = 2$  as well as the smaller  $L = 0$  cross-sections. This is also plotted on a linear scale (right), to show the convergence behaviour of the  $N = 120$ ,  $N = 100$  and  $N = 80$  calculations, not visible on a logscale.



[7] P. M. Bergstrom, T. Surić, K. Pisk, and R. H. Pratt, Phys. Rev. A **48**, 1134 (1993), URL <http://link.aps.org/doi/10.1103/PhysRevA.48.1134>.

[8] H. R. Sadeghpour and A. Dalgarno, J. Phys. B **25**, 4801 (1992), URL <http://stacks.iop.org/0953-4075/25/i=22/a=015>.

[9] E. G. Drukarev, A. I. Mikhailov, and I. A. Mikhailov, Phys. Rev. A **82**, 023404 (2010), URL <http://dx.doi.org/10.1103/PhysRevA.82.023404>.